Energy Proceedings
Vol 57, 2025
ISSN 2004-2965

Corrosion Mechanism of Cr-containing Steel in Water-Saturated Supercritical CO_2 with SO_2 Impurity

Wei Zhang [1], Chunxia Zhang [2, 3], Zehui Zhao [1], Pei Wang [1], Yongyang Zhao [1], Hongxin Ding [1], Yong Xiang [1*]

1 Laboratory for Low Carbon Energy Equipment and Materials Protection, China University of Petroleum, Beijing 102249, China

2 Baoshan Iron& steel CO., Ltd., Shanghai, 201999, China
3 State Key Laboratory of Oil and Gas Equipment, Shanghai, 201999, China
(*Corresponding Author: xiangy@cup.edu.cn)

ABSTRACT

In CO_2 energy storage systems, the working fluid CO_2 contains impurities (H_2O, SO_x) from capture processes, leading to severe equipment corrosion issues that threatens the system stability. In this study, we investigated the corrosion behavior of N80, 3Cr, 9Cr and 13Cr steels in water-saturated supercritical CO_2 (s-CO_2) with 60 ppmv SO_2 at 120°C and 20 MPa to simulate the operating conditions of CO_2 energy storage applications. Multi-scale test methods were employed to systematically reveal the corrosion mechanism of the materials. Uniform corrosion rates were determined using weight-loss measurements, the surface morphology of corrosion products was characterized through scanning electron microscopy (SEM), energy dispersive X-ray spectroscopy (EDS), X-ray diffractometry (XRD), and the characteristics of pitting corrosion was measured by laser confocal microscopy. The results showed that for uniform corrosion, the uniform corrosion rates were measured as 0.170 mm/a for N80 steel and 0.167 mm/a for 3Cr steel, indicating nearly identical corrosion behavior. In comparison, the rates significantly decreased to 0.079 mm/a for 9Cr steel and 0.015 mm/a for 13Cr steel, demonstrating the corrosion resistance enhancement with increasing Cr content. For localized corrosion, all Cr-containing steels except 13Cr exhibited a significant tendency for pitting corrosion. Specifically, for steels with Cr content below 13%wt, the maximum pitting rate demonstrated a positive correlation with Cr content. N80 steel displayed the lowest pitting factor, attributable to its highest uniform corrosion rate. For the corrosion product scales, pits and cracks were observed on the surfaces of all tested steels. XRD analysis revealed that the corrosion product on 13Cr steel contained solely $FeSO_3 \cdot 3H_2O$, while those on N80, 3Cr, and 9Cr steels contained both $FeCO_3$ and $FeSO_3 \cdot 3H_2O$. Cross-sectional EDS line scan analysis demonstrated that apart from differences in corrosion product film thickness, the structural distinction between N80 steel and high-Cr steels stemmed from a thin Cr-rich layer formed at the surface, where Cr content differences were identified. This study indicates that Cr-containing steels pose a corrosion risk under water-saturated supercritical CO_2 environment with SO_2 impurity.

Keywords: CCUS, supercritical CO_2, SO_2, uniform corrosion, localized corrosion, Cr steel

1. INTRODUCTION

Fossil fuels remain a fundamental pillar supporting the development and progress of modern civilization. However, their non-renewable nature and the emission of greenhouse gases, primarily carbon dioxide (CO_2), during combustion have triggered global concern and debate. Carbon capture, utilization and storage (CCUS) technologies not only reduce CO_2 emissions but also offer promising strategies for converting CO_2 into renewable fuels or energy carriers through specific technical pathways, thereby contributing to the realization of a low-carbon economy and sustainable development.

In recent years, among the various CCUS technologies, CO_2-based energy storage technologies have attracted growing attention. Systems such as metal-CO_2 batteries[1], electrothermal energy storage with CO_2 cycles[2], and compressed CO_2 energy storage[3] have demonstrated the potential to store energy efficiently and reduce significant energy waste. However, corrosion and material degradation remain major threats to the safety and service life of such

This is a paper for International CCUS Conference 2025 (ICCUSC 2025), May 28-29, 2025, Beijing, China.

systems[4]. For example, stainless steel bipolar plates in metal-CO_2 batteries are susceptible to corrosion; similarly, carbon steel or stainless steel containers used in electrothermal energy storage with CO_2 cycles suffer from corrosion, and both the cold and hot tanks also have this risk[5]; In the compressed CO_2 energy storage system, both the CO_2 storage tanks and the gas pipelines are at risk of corrosion. Due to technical and economic limitations, corrosive impurities such as water and carbon source impurities, are often present in captured CO_2, posing serious challenges to the long-term and large-scale application of CO_2 energy storage technologies[6].

Among these impurities, sulfur oxides (SO_x) are considered as one of the primary threats causing the aggravation of corrosion severity. In particular, from the CO_2 captured after the combustion of fossil fuels containing sulfur, SO_2 is difficult to remove at a low cost due to its excessively high concentration, making it a particularly troublesome corrosive agent[7-10]. The DY-NAMIS guideline recommends controlling SO_2 levels below 100 ppmv. Zeng et al.[10] reported that the influence of SO_2 in supercritical CO_2 is complex, as SO_2 can dissolve in water to form an acidic liquid film that promotes corrosion of pipeline steels via oxidation and sulfidation. Table 1 summarized current corrosion data on steels exposed to CO_2 containing SO_2. The data clearly indicated that water content significantly influenced the corrosion rate in SO_2-CO_2 systems. When the concentration difference of SO_2 was within one order of magnitude, the corrosion rates under water-saturated and unsaturated conditions differed by more than one order of magnitude. Hua et al.[11] investigated the effect of critical water content and found that reducing water content was more effective than lowering SO_2 concentration in mitigating corrosion risk. Farelas et al.[12] observed that in water-unsaturated conditions, SO_2-CO_2 systems tended to cause severe pitting corrosion. Furthermore, Hua et al.[13] studied the corrosion behavior of steels with varying Cr content under O_2-SO_2-CO_2 environments at relatively low temperature and pressure, and found that X65 steel exhibited better corrosion resistance than 1Cr and 5Cr steels, but lower than that of 13Cr steel, suggesting the possibility of a critical threshold for corrosion resistance based on Cr content.

Despite the growing number of research, data on the corrosion behavior of different Cr-containing steels under high-temperature, high-pressure in supercritical CO_2 environments with SO_2 impurities remain limited. In particular, the mechanisms of pitting corrosion in high-Cr steels remain unclear. To address this gap and better distinguish the corrosion resistance of different steels, this study conducts high-pressure autoclave experiments under water-saturated conditions. The aim is to clarify the corrosion behavior of SO_2 on steels with different Cr content and to explore the existence of a critical Cr threshold under harsh conditions.

Tab.1 Summary of corrosion research on s-CO_2 with SO_2 impurity

T (°C)	P (MPa)	Materials	t (h)	SO_2 (ppmv)	O_2 (ppmv)	H_2O (ppmv)	Corrosion rate (mm/a)	Ref.
50	10	X65	120	1000	0	Sat.	0.469	[9]
35	8	X65	48	100	20	Sat.	0.72	[11]
25	10	X65	240	500	0	1220	0.02	[14]
35	8	13Cr	48	100	0	Sat.	0.01	[15]
25	10	X65	336	100	0	488	<0.005	[7]
25	10	X65	336	344	0	488	<0.005	[7]
25	8	X65	24	100	0	650	~0 (2.4 mm/a localized)	[12]
50	8	X65	24	10000	0	650	3.48	[16]
40	10	X70	48	500	0	Sat.	1.10	[17]
35	8	X65	48	100	20	Sat.	0.72	[13]
35	8	1Cr	48	100	20	Sat.	0.79	[13]
35	8	5Cr	48	100	20	Sat.	0.79	[13]
35	8	13Cr	48	100	20	Sat.	0.01	[13]

2. EXPERIMENT

2.1 Materials preparation

Based on the gradient of Cr content, N80, 3Cr, 9Cr, and 13Cr steels were selected as the experimental materials in this study. The samples were divided into two groups depending on the analysis purpose. Larger samples (40 mm × 8 mm × 4 mm) were used for SEM/EDS characterization, weight loss measurements and 3D

surface morphology analysis, while smaller ones (10 mm × 10 mm × 5 mm) were prepared for cross-sectional morphology analysis and XRD testing. The chemical compositions of all materials were listed in Table 2.

Prior to corrosion testing, all samples were subjected to surface pretreatment. First, the samples were degreased in acetone, rinsed with deionized water and absolute ethanol, and then dried using nitrogen gas (99.999% purity). Then, the surfaces were polished using SiC sandpaper up to 1000 grit, followed by further cleaning with acetone and ethanol to remove any remaining grease or water, and finally dried with nitrogen. The sample dimensions were measured using a vernier caliper with a precision of 0.01 mm, and the weights were recorded using an electronic balance accurate to 0.0001 g.

Then, 100 mL of the deoxygenated water was poured into the autoclave, and the samples were fixed onto a custom holder. After sealing the autoclave, the gas space above the solution was further deoxygenated with nitrogen for 30 minutes. The test gas mixture (5% SO_2 + 95% CO_2) was then introduced at 0.04 MPa at 35°C. The temperature was increased to 120°C, and CO_2 was introduced until the system reached 20 MPa. Corrosion tests were carried out under these conditions for 7 days. It was assumed that SO_2 had negligible influence on the overall density of the gas mixture and its solubility in water. The injection pressure of the gas mixture was calculated as follows: first, the concentration of the impurity gas (SO_2) was determined based on its partial pressure. Then, the moles quantity of CO_2 in the supercritical phase was calculated based on its density at 120°C and 20 MPa,

Tab. 2. Chemical compositions of Cr steels (wt.%)

Materials	C	Si	Mn	Mo	Cr	Cu	Ni	P	S
N80	0.28	0.25	1.4	-	<0.1	-	-	0.015	0.003
3Cr	0.26	0.3	0.8	0.3	3	-	-	0.012	0.002
9Cr	0.15	0.3	0.5	-	9	-	0.5	0.012	0.003
13Cr	0.1	0.4	0.5	-	12.5	-	1.5	0.015	0.003

2.2 Experimental set-up and test procedures

Corrosion tests were conducted using a high-pressure autoclave system. A schematic diagram of the experimental set-up was shown in Figure 1, which included gas cylinders, booster pump, autoclave, and exhaust gas treatment unit. The autoclave (3L, made of Hastelloy C-276) was manufactured by Wuxi Angong Technology. The test gas mixture consisted of 5% SO_2 and 95% CO_2, and the purity of the CO_2 gas cylinder was 99.999%. According to the CO_2-H_2O solubility model, 100 mL of deionized water was added to ensure a water-saturated supercritical CO_2 environment. 2 L volume of deionized water was deoxygenated using nitrogen for 2 hours.

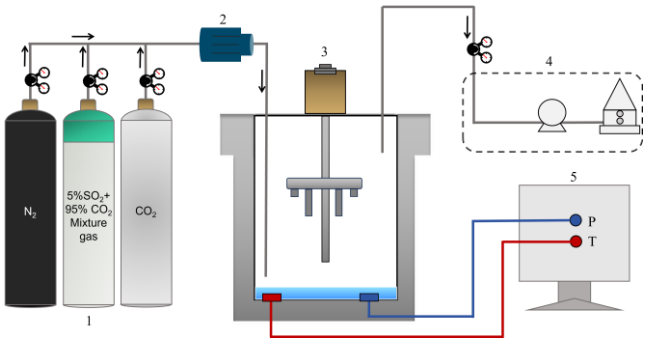

Fig. 1. Experimental set-up for corrosion test: (1) gas cylinders, (2) booster pump, (3) autoclave, (4) exhaust gas treatment unit, (5) temperature and pressure control system

neglecting CO_2 dissolved in the aqueous phase. The number of moles of SO_2 was calculated based on the concentration of the impurity gas. Finally, calculated the pressure required for the mixture gas in the gaseous phase space at 35°C. Table 3 presents the experimental test matrix for the autoclave system.

Tab. 3. Corrosion conditions matrix

Test	T (°C)	P_{tot} (MPa)	SO_2 (MPa)	Water (mL)	Immersion time (h)
N80 3Cr 9Cr 13Cr	120	20	1.2×10^{-3} (60 ppmv)	100	168

After the experiment, the exhaust gas was treated using an absorption purification device to meet environmental safety requirements. Then, the samples were removed, rinsed with deionized water and ethanol, and dried with nitrogen (99.999%). For cross-section analysis, 10 mm × 10 mm × 5 mm samples were embedded in epoxy resin and cured in molds. After curing, the cross-sectional surface was polished for further analysis.

2.3 Methods

To better study the corrosion mechanisms of Cr-containing steels, surface corrosion products were

analyzed using a field emission scanning electron microscope (FEI Quanta 200F) coupled with energy-dispersive X-ray spectroscopy (EDS). X-ray diffraction (XRD) was performed using a Rigaku Ultima IV diffractometer equipped with a Cu-Kα source (λ = 1.5406 nm), operated at 40 kV and 40 mA. The scan range was 5-90° with a scan rate of 4°/min.

The samples were subjected to acid washing with Clarke solution (1000 mL HCl + 20 g Sb_2O_3 + 50 g $SnCl_2$) at 25°C for 5 minutes. According to ASTM G1-03, the uniform corrosion rate was calculated using the weight loss method as shown in Equation (1):

$$CR = \frac{8.76 \times 10^4 \Delta m}{\rho \cdot A \cdot t} \quad (1)$$

where *CR* is the corrosion rate (mm/a), *Δm* is the weight loss (g), *ρ* is the density of the sample (g/cm^3), *A* is the surface area (cm^2), and *t* is the exposure time (h).

To evaluate the number and depth of corrosion pits, the surface of the sample with the product film removed were examined using laser scanning confocal microscopy (LSCM). Based on NACE SP0775-2023 and ASTM G46-21 standards, the maximum pitting rate (*PR*) and pitting factor (*PF*) were calculated using Equations (2) and (3):

$$PR = \frac{8.76 \times (h + \Delta\delta)}{t} \quad (2)$$

$$PF = \frac{\text{deepest mental peneration}}{\text{average mental penetration}} \quad (3)$$

where *h* is the pit depth (μm), and *Δδ* represents the uniform corrosion thickness (μm). The pitting factor was derived from the ratio of maximum pitting rate to the average corrosion rate.

3. RESULTS AND DISCUSSION

3.1 Effect of SO_2 on the corrosion rate

Figure 2 showed the uniform corrosion rates of steels with different Cr content in supercritical CO_2 with 60ppmv SO_2. The corrosion rates followed the order: N80 > 3Cr > 9Cr > 13Cr, indicating that corrosion resistance improved with increasing Cr content. Quantitatively, when Cr content increased to 3 wt.%, the change in corrosion rate was negligible. N80 and 3Cr exhibited rates of 0.170 mm/a and 0.167 mm/a, respectively. However, as Cr content further increased to 9 wt.% and 13 wt.%, the corrosion rates dropped significantly to 0.079 mm/a and 0.015 mm/a, respectively. This trend suggested the presence of a critical Cr content threshold influencing corrosion resistance in SO_2-containing supercritical CO_2 environments, possibly around 3 wt.%.

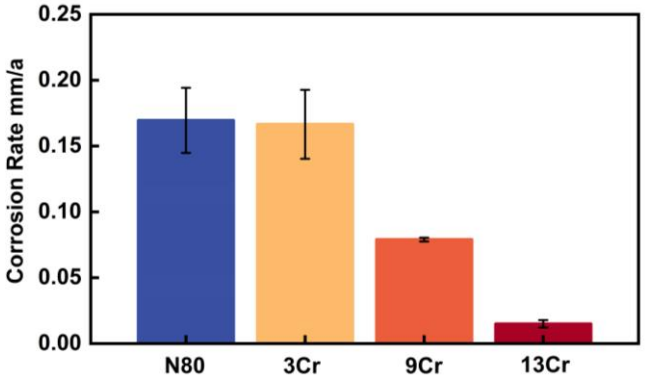

Fig. 2. Uniform corrosion rate of different Cr-containing steels in s-CO_2 at 120°C and 20 MPa with 60 ppmv SO_2

3.2 Effect of SO_2 on corrosion product morphology and composition

Figure 3 showed cross-sectional morphologies of the tested steels. Arrows in Figures 3a-d indicated EDS line scan paths, and Figures 3e and 3f presented mapping scan results for N80 and 13Cr, respectively. The results showed that in Figure 3a, localized corrosion was observed on the N80 steel. The line scanning analysis indicated that there was an S element enrichment (up to 10 wt.%) on N80 within 5-10 μm from the substrate. The S element content decreased to within 5 wt% at around 5 μm near the epoxy. Combined with the XRD results in Figure 4, the corrosion products were identified as $FeCO_3$ and $FeSO_3 \cdot 3H_2O$. $FeCO_3$ exhibited anion selectivity[18], allowing anion to diffuse through the porous film and cause metal dissolution, leading to sulfur accumulation near the metal interface. In N80 localized corrosion zones, as shown in Figure 3e, little sulfur was detected.

For 3Cr steel, as shown in Figure 3b, cracks were observed in the corrosion product layer. The line scanning analysis of 3Cr indicated that there was a Cr-rich area of approximately 10 μm near the substrate. Although Cr-rich product layers are typically protective, 3 wt.% Cr content was insufficient to form a dense barrier[19] to protect substrate. Instead, the porous Cr-rich product layer provided less protection than a crystalline $FeCO_3$ layer, which could have explained the similar uniform corrosion rates of N80 and 3Cr[19]. The Cr-rich layer exhibited cation selectivity[19]. A sulfur-rich zone (up to 26.54 wt.%) was found near the epoxy at a depth of approximately 5 μm, while only one sulfur peak (6.17 wt.%) was observed in the inner corrosion product layer.

For 9Cr steel, as shown in Figure 3c, no obvious pits or cracks were found, suggesting the formation of a dense corrosion product film. The inner layer showed high Cr content, while the outer layer contained almost

none. Figures 3d and 3f showed that no obvious corrosion product film was formed on the surface of 13Cr.

Figure 4 showed the XRD analysis results of steels with different Cr content after 168h exposure to

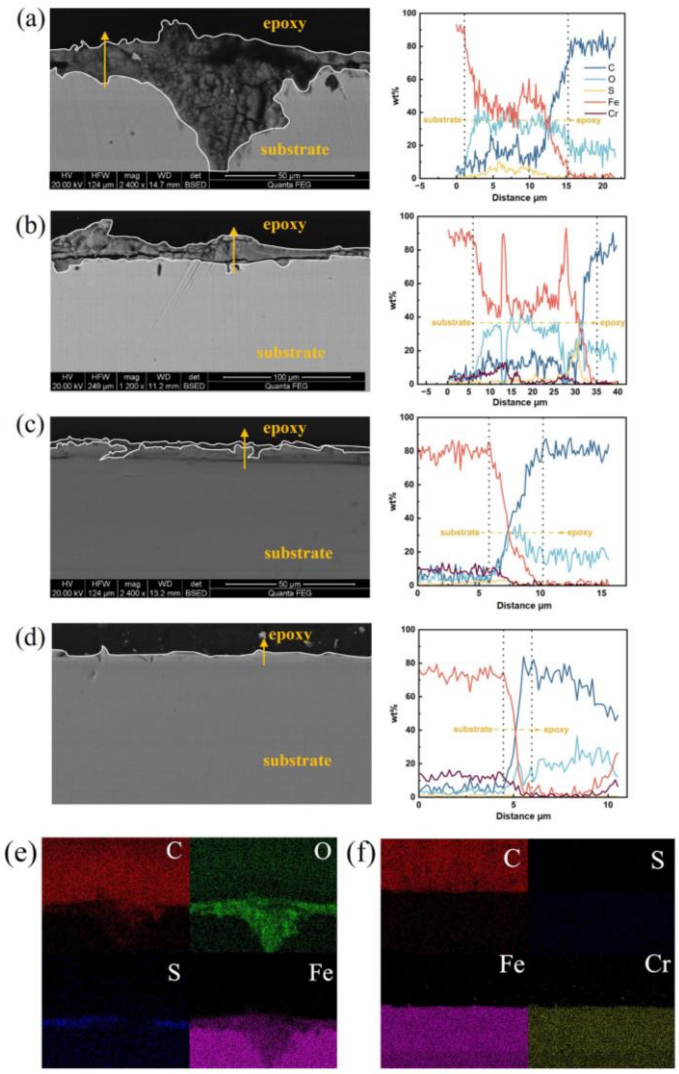

Fig. 3. SEM and EDS results of the cross-sectional morphologies of different Cr content steels in s-CO_2 at 120°C and 20 MPa with 60ppmv SO_2: (a) N80, (b) 3Cr, (c) 9Cr, (d) 13Cr, (e) EDS mapping of N80, (f) EDS mapping of 13Cr

supercritical CO_2 with 60 ppmv SO_2. The results showed that $FeCO_3$ and $FeSO_3 \cdot 3H_2O$ corrosion products were formed on the surfaces of N80, 3Cr, and 9Cr steels, while only $FeSO_3 \cdot 3H_2O$ was detected on the surface of 13Cr steel. $FeSO_3$ has also been identified in previous studies under SO_2-containing environments by Choi[16], Xiang[20], and Hua[15], and has been reported to exhibit poor protective properties.

However, Cr-containing corrosion products were not detected in the XRD results. This suggests that the Cr-containing species were either amorphous or that the Cr-rich layer was too thin to be detected by XRD.

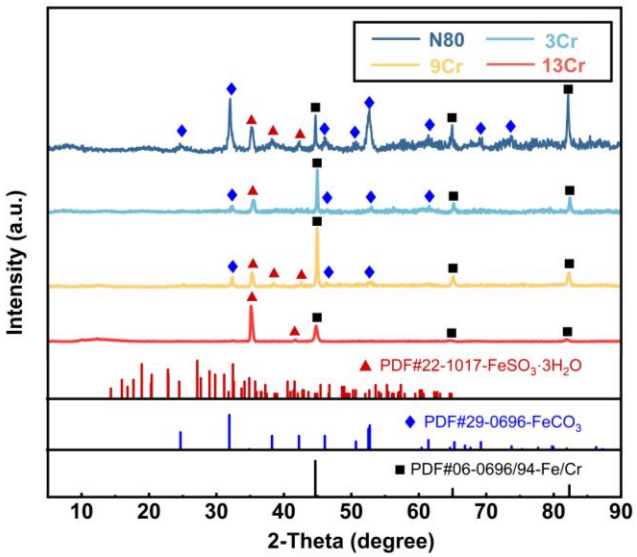

Fig. 4. XRD results of different Cr content steels in s-CO_2 at 120°C and 20 MPa with 60 ppmv SO_2

3.3 Effect of SO_2 on the localized corrosion

Figure 5 presented the corresponding pitting rates calculated from the deepest pits. Figure 6 showed the 3D surface morphology of the maximum pitting sites on each steel after removal of corrosion products. All materials exhibited varying degrees of localized

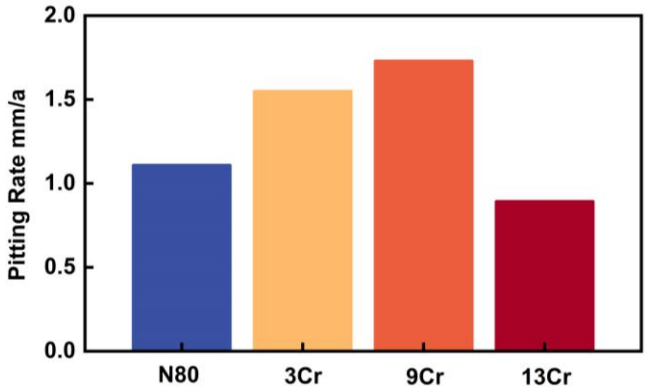

Fig. 5. Pitting rate of different Cr content steels in s-CO_2 at 120°C and 20 MPa with 60 ppmv SO_2

corrosion. When Cr content was ≤ 9 wt.%, increasing Cr led to deeper and wider pits and higher pitting rates. However, when Cr content exceeded 9 wt.%, the 13Cr steel exhibited narrower and more elongated pits, with the lowest pitting rate at 0.892 mm/a. The pitting factor increased with Cr content, with values of 6.54, 9.30, and 21.88 for N80, 3Cr, and 9Cr, respectively, indicating that

the tendency for pitting became more severe as Cr content increased. For 13Cr, the pitting factor was relatively high due to its extremely low uniform corrosion rate, making it an unreliable indicator of pitting susceptibility in this experiment.

3.4 Insights into SO_2 reaction mechanism

3.4.1 Reaction mechanism of N80 steel

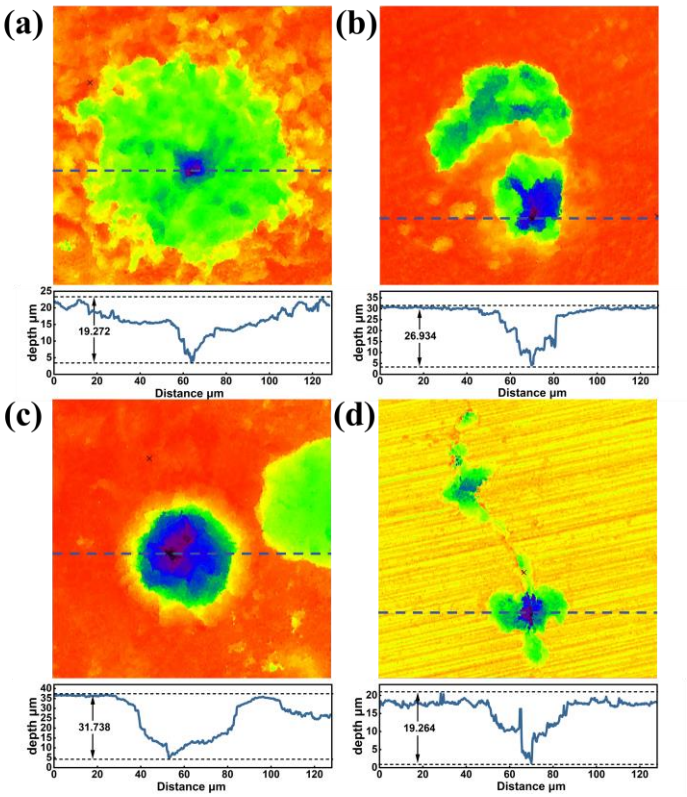

Fig. 6. 3D surface morphologies of different Cr-containing steels after removal of corrosion products in s-CO_2 at 120°C and 20 MPa with 60 ppmv SO_2: (a) N80, (b) 3Cr, (c) 9Cr, (d) 13Cr

In water-saturated supercritical CO_2, corrosion mechanisms can be categorized as either electrochemically or chemically dominated, depending on whether a thin liquid film forms on the metal surface[21, 22]. The presence of SO_2 was reported to reduce the solubility of H_2O in CO_2[23], promoting the formation of such thin liquid films. Li et al.[23] suggested that corrosion in s-CO_2 with SO_2 environments was primarily governed by electrochemical reactions. The thin liquid film served as a medium for ionic and electronic transport through diffusion in the metal, corrosion products, and bulk solution. Then CO_2 and SO_2 undergo dissolution and ionization in the thin liquid film, with possible reactions described in Equations (4)-(9). Xiang et al.[20] concluded that in high-SO_2 environments (0.2-2 mol%), corrosion was dominated by SO_2 rather than CO_2. In this study, the SO_2 concentration was only 60 ppmv, so it was likely that both CO_2 and SO_2 contributed significantly to the corrosion process. Thus, reactions (4)-(7) were considered[8, 13, 16, 17, 20, 23, 24]. SO_2 dissolved in water to form sulfurous acid[16], which lowered the pH of the thin film and significantly increased the acidity of the corrosion environment. In this acidic solution, Fe dissolution was accelerated and served as the primary anodic reaction, as shown in Reaction (11)[25]. In the acidic, oxygen-depleted environment, the dominant cathodic reaction was hydrogen evolution, as shown in Reaction (10)[25].

CO_2 dissolution and ionization reactions:

$$CO_{2(g)} \leftrightarrow CO_{2(aq)} \quad (4)$$

$$CO_2 + H_2O \leftrightarrow H_2CO_3 \quad (5)$$

$$H_2CO_3 \leftrightarrow H^+ + HCO_3^- \quad (6)$$

$$HCO_3^- \leftrightarrow H^+ + CO_3^{2-} \quad (7)$$

When SO_2 is introduced into the system, the possible reactions:

$$H_2O + SO_2 \leftrightarrow HSO_3^- + H^+ \quad (8)$$

$$HSO_3^- \leftrightarrow H^+ + SO_3^{2-} \quad (9)$$

Cathodic reaction:

$$2H^+ + 2e^- \leftrightarrow H_2 \quad (10)$$

Anodic reaction:

$$Fe \rightarrow Fe^{2+} + 2e^- \quad (11)$$

According to Figure 4, the primary corrosion products in the presence of SO_2 were $FeCO_3$ and $FeSO_3 \cdot 3H_2O$. Their formation processes are described in reaction 12, 14-16[8, 13, 16, 17, 20, 23, 24].

$FeSO_3$ and $FeCO_3$ precipitation reaction:

$$Fe^{2+} + SO_3^{2-} \rightarrow FeSO_3 \quad (12)$$

$$S_{FeSO_3} = \frac{c_{Fe^{2+}} \cdot c_{SO_3^{2-}}}{K_{sp,FeSO_3}} \quad (13)$$

$$Fe^{2+} + CO_3^{2-} \rightarrow FeCO_3 \quad (14)$$

$$Fe^{2+} + 2HCO_3^- \rightarrow Fe(HCO_3)_2 \quad (15)$$

$$Fe(HCO_3)_2 \rightarrow FeCO_3 + CO_2 + H_2O \quad (16)$$

$$S_{FeCO_3} = \frac{c_{Fe^{2+}} \cdot c_{CO_3^{2-}}}{K_{sp,FeCO_3}} \quad (17)$$

where S_i is the supersaturation of component i in reaction 13, 17, $c_{Fe^{2+}}$, $c_{CO_3^{2-}}$, $c_{SO_3^{2-}}$ represent the concentrations of Fe^{2+}, CO_3^{2-}, SO_3^{2-} in solution (mol/L), and $K_{sp,FeCO_3}$, $K_{sp,FeSO_3}$ are the solubility products (mol^2/L^2).

When the concentrations of Fe^{2+}, CO_3^{2-}, and SO_3^{2-} increased, resulting in S_{FeCO_3}, S_{FeSO_3} >1, $FeCO_3$ and $FeSO_3$ precipitate on the metal surface. Observations of N80 steel indicated that the resulting mixed layer was

porous and loosely structured, offering poor protective performance.

3.4.2 Reaction mechanism of high-Cr steel

Regarding the reaction mechanism of high-Cr steels, the main difference from the corrosion products of low-Cr steel like N80 and 3Cr lies in the presence of a dense Cr-rich layer in the inner mixed product layer. The corrosion results showed that a Cr content of 3 wt.% was insufficient to form a dense Cr-rich layer, although a loosely structured layer could still offer some resistance to the diffusion of SO_3^{2-} ions. When Cr content exceeded 9 wt.%, a compact Cr-rich passive film was formed, which significantly improved resistance to uniform corrosion. The possible reaction pathway of the Cr-rich layer is illustrated in Reaction (18) and (19)[19].

$$Cr \rightarrow Cr^{3+} + 3e^{-} \quad (18)$$

$$Cr^{3+} + 3OH^{-} \rightarrow Cr(OH)_3 \quad (19)$$

The overall corrosion process of high-Cr steels in water-saturated supercritical CO_2 with SO_2 is illustrated in Figure 7. Initially, the presence of SO_2 reduces water solubility in supercritical CO_2, promoting the formation of condensed water on the metal surface and shifting the corrosion mechanism toward an electrochemical process. A thin water film forms on the steel surface, into which CO_2 and SO_2 dissolve, undergo hydration, and ionize to generate HCO_3^-, CO_3^{2-}, SO_3^{2-}, H^+, and OH^- ions. The anodic dissolution of the steel substrate produces Fe^{2+} and Cr^{3+} ions. These ions contribute to the initial formation of a porous corrosion product layer composed mainly of $FeSO_3$ and Cr-rich layer at the substrate-film interface. With continued exposure, $FeCO_3$ begins to precipitate within the pores of $FeSO_3$ and at the $FeSO_3$-substrate interface. This $FeCO_3$ is initially amorphous and offers limited protection. Over time, the deposition of $FeCO_3$ and $FeSO_3$ gradually leads to a more compact and protective corrosion product layer.

However, a higher Cr content could lead to more severe pitting corrosion. This may be related to the failure of weak areas in the corrosion product film. Khamme[26] demonstrated that under certain acidic conditions, H^+ ions can lead to the dissolution of the passive film. For 13Cr steel, the surface showed few corrosion products, and $FeCO_3$ was not detected by XRD. This indicated the formation of a Cr-rich passive layer on the steel substrate. Owing to the cation selectivity of the Cr-rich passive layer, this layer prevents corrosive species from diffusing through and reacting with Fe to form $FeCO_3$ precipitates. As a result, the localized supersaturation of $FeCO_3$ remains below 1, which inhibits the nucleation and growth of $FeCO_3$. Meanwhile, the presence of pitting on 13Cr indicates a possible localized failure of the passive film.

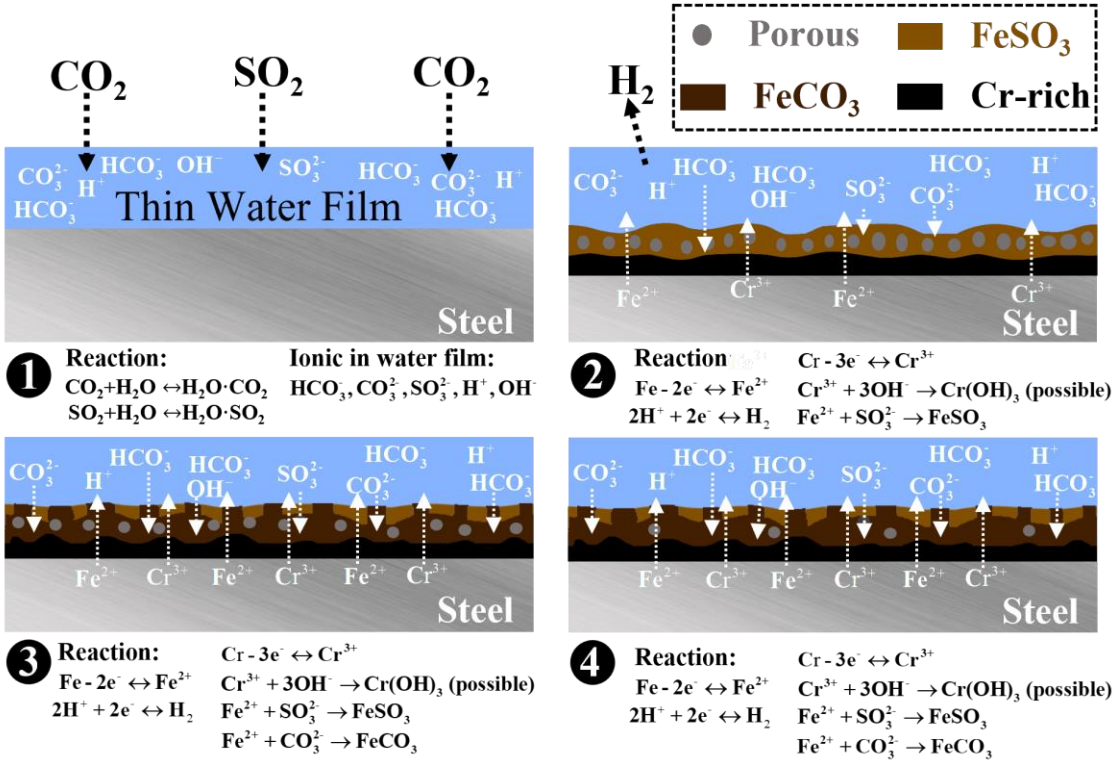

Fig. 7. Corrosion mechanism diagram of high-Cr steel in s-CO_2 at 120°C and 20 MPa with 60 ppmv SO_2

4. CONCLUSIONS

This study investigated the corrosion mechanism of steels with varying Cr content in water-saturated supercritical CO_2 with 60 ppmv SO_2. The main conclusions are as follows:

1) Corrosion product films: $FeSO_3 \cdot 3H_2O$ was identified on all tested steels, while $FeCO_3$ was detected on N80, 3Cr, and 9Cr but not on 13Cr. A Cr-rich layer was observed in the inner mixed product layer for high-Cr steel. The mixed layer of $FeCO_3$ and $FeSO_3 \cdot 3H_2O$ was porous and poorly protective. For 3Cr steel, a loosely structured Cr-rich layer partially hindered SO_3^{2-} diffusion, while a dense Cr-rich layer formed on 9Cr and 13Cr provided effective substrate protection.

2) Uniform corrosion: The uniform corrosion rate of Cr-containing steels exhibited a non-linear decreasing trend with increasing Cr content. A Cr content of 3 wt.% appeared to be a critical threshold. When Cr ≤ 3 wt.%, the Cr-rich layer remained loose or was difficult to detect, resulting in similarly high corrosion rates among N80 and 3Cr steels. In contrast, when Cr > 3 wt.%, a thinner and denser corrosion product film formed, and the corrosion rate dropped significantly.

3) The acidic environment weakened the protective ability of the corrosion product film, resulting in pitting at weak sites. When Cr ≤ 9 wt.%, both the pitting rate and pitting factor increased with Cr content, indicating an increasing tendency for localized corrosion. Notably, 13Cr exhibited the lowest pitting rate (0.892 mm/a), reflecting improved resistance to localized corrosion.

ACKNOWLEDGEMENT

This work was financially Supported by the National Science and Technology Major Project of China for New Oil and Gas Exploration and Development (grant number: 2024ZD1406603), the National Natural Science Foundation of China (grant number: 52271082).

DECLARATION OF INTEREST STATEMENT

The authors declare that they have no known competing financial interests or personal relationships that could have appeared to influence the work reported in this paper. All authors read and approved the final manuscript.

REFERENCE

[1] XIE J, ZHOU Z, WANG Y. Metal-CO_2 batteries at the crossroad to practical energy storage and CO_2 recycle [J]. Advanced Functional Materials, 2020, 30(9): 1908285.

[2] MERCANGöZ M, HEMRLE J, KAUFMANN L, et al. Electrothermal energy storage with transcritical CO_2 cycles [J]. Energy, 2012, 45(1): 407-415.

[3] LIU Z, YANG X, JIA W, et al. Justification of CO_2 as the working fluid for a compressed gas energy storage system: a thermodynamic and economic study [J]. Journal of Energy Storage, 2020, 27: 101132.

[4] SAJI V S. Corrosion and materials degradation in electrochemical energy storage and conversion devices [J]. ChemElectroChem, 2023, 10(11): e202300136.

[5] NIETO-MAESTRE J, MUñOZ-SáNCHEZ B, FERNáNDEZ A G, et al. Compatibility of container materials for Concentrated Solar Power with a solar salt and alumina based nanofluid: A study under dynamic conditions [J]. Renewable Energy, 2020, 146: 384-396.

[6] WEI L, ZHANG Y, PANG X, et al. Corrosion behaviors of steels under supercritical CO_2 conditions [J]. Corrosion Reviews, 2015, 33(3-4): 151-174.

[7] DUGSTAD A, HALSEID M, MORLAND B. Effect of SO_2 and NO_2 on corrosion and solid formation in dense phase CO_2 pipelines [J]. Energy Procedia, 2013, 37: 2877-2887.

[8] HUA Y, BARKER R, NEVILLE A. Understanding the influence of SO_2 and O_2 on the corrosion of carbon steel in water-saturated supercritical CO_2 [J]. Corrosion, 2015, 71(5): 667-683.

[9] SUN C, SUN J, WANG Y, et al. Synergistic effect of O_2, H_2S and SO_2 impurities on the corrosion behavior of X65 steel in water-saturated supercritical CO_2 system [J]. Corrosion Science, 2016, 107: 193-203.

[10] ZENG Y, LI K. Influence of SO_2 on the corrosion and stress corrosion cracking susceptibility of supercritical CO_2 transportation pipelines [J]. Corrosion Science, 2020, 165: 108404.

[11] HUA Y, BARKER R, NEVILLE A. The influence of SO_2 on the tolerable water content to avoid pipeline corrosion during the transportation of supercritical CO_2 [J]. International Journal of Greenhouse Gas Control, 2015, 37: 412-423.

[12] FARELAS F, CHOI Y, NEŠIĆ S. Corrosion behavior of API 5L X65 carbon steel under supercritical and liquid carbon dioxide phases in the presence of water and sulfur dioxide [J]. Corrosion, 2013, 69(3): 243-250.

[13] HUA Y, BARKER R, BERMPERIDIS G, et al. Comparison of corrosion behavior of X65, 1Cr, 5Cr and 13Cr steels in water-containing supercritical CO_2 environments with SO_2/O_2; proceedings of the NACE CORROSION, F, 2016 [C]. NACE.

[14] DUGSTAD A, HALSEID M. Internal corrosion in dense phase CO_2 transport pipelines-state of the art and the need for further R&D; proceedings of the NACE CORROSION, F, 2012 [C]. NACE.

[15] HUA Y, JONNALAGADDA R, ZHANG L, et al. Assessment of general and localized corrosion behavior of X65 and 13Cr steels in water-saturated supercritical

CO_2 environments with SO_2/O_2 [J]. International Journal of Greenhouse Gas Control, 2017, 64: 126-136.
[16] CHOI Y-S, NEŠIC S. Effect of water content on the corrosion behavior of carbon steel in supercritical CO_2 phase with impurities; proceedings of the NACE CORROSION, F, 2011 [C]. NACE.
[17] WANG W, SHEN K, TANG S, et al. Synergistic effect of O_2 and SO_2 gas impurities on X70 steel corrosion in water-saturated supercritical CO_2 [J]. Process Safety Environmental Protection, 2019, 130: 57-66.
[18] CHEN C, LU M, SUN D, et al. Effect of chromium on the pitting resistance of oil tube steel in a carbon dioxide corrosion system [J]. Corrosion, 2005, 61(06).
[19] WEI L, GAO K. Understanding the general and localized corrosion mechanisms of Cr-containing steels in supercritical CO_2-saturated aqueous environments [J]. Journal of Alloys Compounds, 2019, 792: 328-340.
[20] XIANG Y, WANG Z, XU C, et al. Impact of SO_2 concentration on the corrosion rate of X70 steel and iron in water-saturated supercritical CO_2 mixed with SO_2 [J]. The Journal of Supercritical Fluids, 2011, 58(2): 286-294.
[21] GUAN X, ZHU T, MACDONALD D D. Application of Electrochemical Noise Analysis in High Subcritical and Supercritical Aqueous System; proceedings of the NACE CORROSION, F, 2006 [C]. NACE.
[22] GUAN X, MACDONALD D. Determination of corrosion mechanisms and estimation of electrochemical kinetics of metal corrosion in high subcritical and supercritical aqueous systems [J]. Corrosion, 2009, 65(6): 376-387.
[23] LI K, ZENG Y. Long-term corrosion and stress corrosion cracking of X65 steel in H_2O-saturated supercritical CO_2 with SO_2 and O_2 impurities [J]. Construction Building Materials, 2023, 362: 129746.
[24] LI C, XIANG Y, LI W. Initial corrosion mechanism for API 5L X80 steel in CO_2/SO_2-saturated aqueous solution within a CCUS system: Inhibition effect of SO_2 impurity [J]. Electrochimica Acta, 2019, 321: 134663.
[25] NEŠIĆ S. Key issues related to modelling of internal corrosion of oil and gas pipelines-A review [J]. Corrosion science, 2007, 49(12): 4308-4338.
[26] KHAMME E, SAKDANUPHAB R. Study of corrosion properties of carbon steel, 304 and 316L stainless steels in sulfuric acid and their degradation products [J]. Journal of Metals, Materials Minerals, 2023, 33(4): 1672-1672.